

## A MEMS Coriolis-Based Mass-Flow-to-Digital Converter for Low Flow Rate Sensing

de Oliveira, Arthur Campos; Pan, Sining; Wiegerink, Remco J.; Makinwa, Kofi A.A.

**DOI**

[10.1109/JSSC.2022.3210003](https://doi.org/10.1109/JSSC.2022.3210003)

**Publication date**

2022

**Document Version**

Final published version

**Published in**

IEEE Journal of Solid-State Circuits

**Citation (APA)**

de Oliveira, A. C., Pan, S., Wiegerink, R. J., & Makinwa, K. A. A. (2022). A MEMS Coriolis-Based Mass-Flow-to-Digital Converter for Low Flow Rate Sensing. *IEEE Journal of Solid-State Circuits*, 57(12), 3681-3692. <https://doi.org/10.1109/JSSC.2022.3210003>

**Important note**

To cite this publication, please use the final published version (if applicable). Please check the document version above.

**Copyright**

Other than for strictly personal use, it is not permitted to download, forward or distribute the text or part of it, without the consent of the author(s) and/or copyright holder(s), unless the work is under an open content license such as Creative Commons.

**Takedown policy**

Please contact us and provide details if you believe this document breaches copyrights. We will remove access to the work immediately and investigate your claim.

***Green Open Access added to TU Delft Institutional Repository***

***'You share, we take care!' - Taverne project***

**<https://www.openaccess.nl/en/you-share-we-take-care>**

Otherwise as indicated in the copyright section: the publisher is the copyright holder of this work and the author uses the Dutch legislation to make this work public.

# A MEMS Coriolis-Based Mass-Flow-to-Digital Converter for Low Flow Rate Sensing

Arthur Campos de Oliveira<sup>1</sup>, Graduate Student Member, IEEE, Sining Pan<sup>2</sup>, Member, IEEE, Remco J. Wiegink<sup>1</sup>, and Kofi A. A. Makinwa, Fellow, IEEE

**Abstract**—This article presents a microelectromechanical system (MEMS) Coriolis-based mass-flow-to-digital converter ( $\Phi$ DC) that can be used with both liquids and gases. It consists of a micromachined Coriolis mass flow sensor and a CMOS interface circuit that drives it into oscillation and digitizes the resulting mass flow information. A phase-locked loop (PLL) drives the sensor at its resonance frequency ( $f_D$ ), while a low  $1/f$  noise switched-capacitor (SC) proportional-integral (PI) controller maintains a constant drive amplitude. Mass flow through the sensor causes Coriolis-force-induced displacements, which are detected by co-integrated sense capacitors. In-phase ( $I$ ) and quadrature ( $Q$ ) components of these displacements are then digitized by two continuous-time delta-sigma modulators (CT- $\Delta\Sigma$ M) with finite impulse response (FIR)-DACs and passive mixers. Their outputs are used to accurately estimate and cancel sense path delay, thus improving sensor stability. To ensure constant sensitivity over a wide range of fluid densities, a background sensitivity tuning (BST) scheme adjusts the sense capacitors' bias voltage as a function of  $f_D$ , which is a good proxy for fluid density. Implemented in a standard 0.18- $\mu\text{m}$  CMOS technology, the interface circuit consumes 13 mW from a 1.8-V supply. The proposed MEMS Coriolis  $\Phi$ DC achieves a state-of-the-art noise floor of 80  $\mu\text{g/h}/\sqrt{\text{Hz}}$  and a zero stability (ZS) of  $\pm 0.31$  mg/h, which is at par with MEMS thermal flow sensors.

**Index Terms**—Capacitive interface, CMOS readout interface, Coriolis mass flow sensor, delta-sigma modulator ( $\Delta\Sigma$ M), flow rate, flowmeter, demodulator, low noise, microelectromechanical systems (MEMS), microfluidics.

## I. INTRODUCTION

FLOW sensors are required in many industrial and microfluidic applications, such as flow cytometry [1], biological/chemical assays [2], and volatile organic compound detection [3], [4]. Their primary function is to translate fluid flow into analog or digital information, thus allowing it to be measured and controlled. However, detecting the low flow rates, often less than 1 g/h, associated with

microfluidic applications requires sensors with high resolution ( $<200$   $\mu\text{g/h}/\sqrt{\text{Hz}}$ ) and low drift ( $<\pm 0.4$  mg/h). They should also be able to maintain good accuracy in the presence of variations in fluid viscosity and density. Last but not least, they should be as small as possible to facilitate their use in a wide range of microfluidic systems, which are often volume constrained.

Flow sensors based on microelectromechanical systems (MEMS) are well suited for microfluidic and low flow industrial applications [5]. Compared with conventional flow sensors, they can be manufactured in volume using wafer-level batch fabrication techniques, which, in turn, reduces process variability and costs. In addition, they can be co-integrated and packaged with CMOS circuitry, which confers ease of use as well as a small system size.

Several MEMS/CMOS flow sensors suited for low flow applications have been reported [6], [7], [8], [9], [10], [11], [12], [13], [14], [15], [16], [17], [18]. Thermal flow sensors [6], [7], [8], [9], [10] are among the most popular. Such sensors typically employ a few temperature sensors located around a heater to measure the temperature asymmetry caused by fluid flow. They have no moving parts and, thus, can achieve high stability and resolution ( $<100$   $\mu\text{g/h}/\sqrt{\text{Hz}}$ ). However, since they sense mass flow indirectly via fluid heat capacity and temperature differences, thermal flow sensors have to be calibrated for use with specific liquids [8] or gases [9], [10] and, consequently, cannot be used for unknown mixtures of fluids. Furthermore, their output tends to saturate at higher flow rates, limiting their dynamic range [8], [10].

Coriolis flow sensors [11], [12], [13], [14], [15], [16], [17], [18], [19], [20], [21], on the other hand, directly measure mass flow by sensing the Coriolis force produced by a flowing mass in a vibrating channel. This force is independent of fluid properties, and so, the same sensor can be used to accurately ( $<\pm 0.5\%$ ) measure the mass flow rate of both liquids and gases. In addition, fluid density can be estimated from the resonance frequency of the vibrating channel [22], [23]. However, commercially available Coriolis flow sensors are made of stainless steel (SS) [21] and so are bulky and expensive. They also suffer from poor stability ( $\pm 10$  mg/h) at low flow rates, since the associated Coriolis forces are quite small and, thus, difficult to detect [24].

In contrast, MEMS Coriolis flow sensors [11], [12], [13], [14], [15], [16], [17], [18], [19] can be much more sensitive. In [12], a sensor intended for low flow rates is presented, but its use of a monocrystalline silicon flow channel limits its mass and stiffness, resulting in low sensitivity and the need

Manuscript received 15 May 2022; revised 29 July 2022 and 13 September 2022; accepted 15 September 2022. Date of publication 14 October 2022; date of current version 28 November 2022. This article was approved by Associate Editor Jens Anders. This work was supported by the research program FLOW+, which is financed by the Dutch Technology Foundation STW and industrial partners Bronkhorst BV and KROHNE. (Corresponding author: Arthur Campos de Oliveira.)

Arthur Campos de Oliveira and Kofi A. A. Makinwa are with the Electronic Instrumentation Laboratory, Department of Microelectronics, Delft University of Technology, 2628 CD Delft, The Netherlands (e-mail: a.camposdeoliveira@tudelft.nl).

Sining Pan is with the Department of Electrical Engineering, Tsinghua University, Beijing 100190, China.

Remco J. Wiegink is with the Integrated Devices and Systems Group, University of Twente, 7522 NB Enschede, The Netherlands.

Color versions of one or more figures in this article are available at <https://doi.org/10.1109/JSSC.2022.3210003>.

Digital Object Identifier 10.1109/JSSC.2022.3210003

for vacuum packaging. Furthermore, it also suffered from a large ( $\pm 200$  mg/h) zero stability (ZS). Bulk-micromachining-based surface channel technology (SCT) [25], [26] enables the fabrication of silicon-rich silicon nitride (SiRN) flow channels with much lower mass and stiffness, resulting in high sensitivity at low flows [16]. In recent work, it has been shown that such sensors can be combined with CMOS circuitry to achieve compact drive and sensing functionality while maintaining high resolution ( $300 \mu\text{g/h}/\sqrt{\text{Hz}}$ ) and low ZS ( $\pm 0.8$  mg/h) [14]. However, sub- $100 \mu\text{g/h}/\sqrt{\text{Hz}}$  noise floor and further reduction of the ZS are required to make MEMS Coriolis a reliable alternative to MEMS thermal flow sensors in low flow and microfluidic applications.

In this work, an extended version of [15], a mass-flow-to-digital converter ( $\Phi$ DC) based on a MEMS Coriolis mass flow sensor is presented. CMOS circuitry is used to implement both its drive loop and readout electronics, while also providing a compact digital-output system. To achieve low ZS, the circuitry is designed to have low  $1/f$  noise, while residual quadrature ( $Q$ )-induced drift is cancelled in the digital domain. The proposed  $\Phi$ DC achieves a noise floor of about  $80 \mu\text{g/h}/\sqrt{\text{Hz}}$  and a ZS of  $\pm 0.31$  mg/h in a 4-Hz bandwidth, which corresponds to a  $3.75\times$  and  $2.6\times$  improvement, respectively, on the state of the art [14].

The rest of this article is organized as follows. Section II briefly introduces the MEMS Coriolis mass flow sensor's working principle and design considerations. Section III presents the proposed sensor interface architecture and some key circuit-level details. In Section IV, measurement results are discussed and compared with other state-of-the-art flow sensors. Finally, Section V concludes this article.

## II. MICROMACHINED CORIOLIS MASS FLOW SENSOR

### A. Operating Principle

The operation of a MEMS Coriolis mass flow sensor is illustrated in Fig. 1. The sensor consists of a suspended vibrating flow channel with two main resonance modes: the drive (twist) and the sense (swing) modes. In the presence of a static magnetic field ( $B$ ), the drive mode is actuated by passing an alternating current ( $i_D$ ) through a metal track at the top of the suspended channel. This generates a Lorentz force ( $F_L = i_D \times B \times L$ ) at the sections [ $L$ , in Fig. 2(a)] of the channel, where  $i_D$  is orthogonal to  $B$  [27], resulting in a drive displacement ( $x_D$ ) at the outer corners of the channel, as shown in Fig. 1(a).

The drive mode can be modeled as a lumped-element mass-spring system with resonance frequency [23]

$$f_D = \frac{1}{2\pi} \sqrt{\frac{k_D}{m_{\text{ch}} + m_f}} = \frac{1}{2\pi} \sqrt{\frac{k_D}{m_{\text{ch}} + \rho V_{\text{ch}}}} \quad (1)$$

where  $k_D$  is the drive mode spring constant,  $m_{\text{ch}}$  is the mass of the empty channel,  $m_f$  is the fluid mass inside the channel,  $V_{\text{ch}}$  is the channel's volume, and  $\rho$  is the fluid density. From (1), it can be seen that the fluid density directly impacts the resonance frequency in proportion to the added fluid mass, allowing  $\rho$  to be estimated by measuring changes in  $f_D$ .

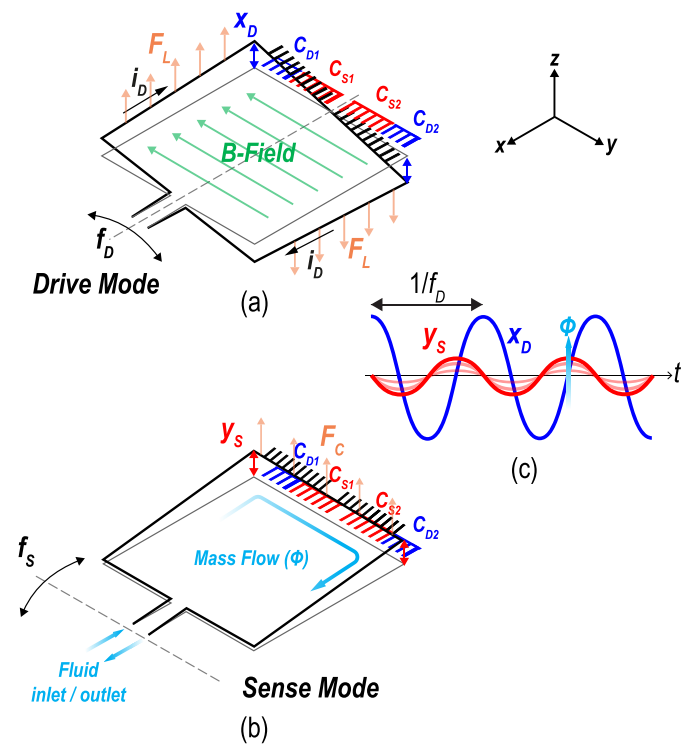


Fig. 1. Operation principle of the MEMS Coriolis mass flow sensor: movement when (a) driven at its drive mode resonance frequency, (b) sense mode is excited by the Coriolis force, and (c) drive ( $x_D$ ) and sense ( $y_S$ ) displacements in the time domain.

Fluid flowing through the channel with a mass flow rate  $\Phi$  will experience a Coriolis force ( $F_C$ ) with amplitude

$$F_C \approx 4\omega_D x_D \Phi. \quad (2)$$

This induces an out-of-plane sense displacement ( $y_S$ ) that is proportional to the drive velocity, thus orthogonal to the drive mode displacement  $x_D$ , and modulated by  $f_D$ , as shown in Fig. 1(b) and (c). The Coriolis force is proportional to  $\Phi$  and is independent of temperature, pressure, flow profile, and fluid properties. From a lumped model of the sense mode, assuming that it is harmonically driven at  $f_D$ , the Coriolis force-induced displacement amplitude  $|y_S|$  can be expressed as follows:

$$|y_S(\omega_D)| \approx \frac{F_C}{k_S \sqrt{\left(1 - \left(\frac{\omega_D}{\omega_S}\right)^2\right)^2 + \left(\frac{\omega_D}{\omega_S Q_S}\right)^2}} \quad (3)$$

where  $k_S$ ,  $\omega_S$ , and  $Q_S$  are the sense mode spring constant, resonance frequency ( $f_S = \omega_S/2\pi$ ), and quality factor, respectively. Since the ratio  $(\omega_D/\omega_S)$  is almost independent of fluid density [18], and the amplitude of  $x_D$  can be regulated, the Coriolis force-induced  $y_S$  can be used as a frequency-dependent measure of mass flow.

From (1) and (3), to accurately sense mass flow and density, the sensor must be operated at  $f_D$ , while the amplitudes of  $y_S$  and  $x_D$  must be sensed and regulated, respectively.

### B. Suspended Channel Design

High sensitivity is desired to measure mass flows below 1 g/h with high resolution. To achieve this, the mass of the

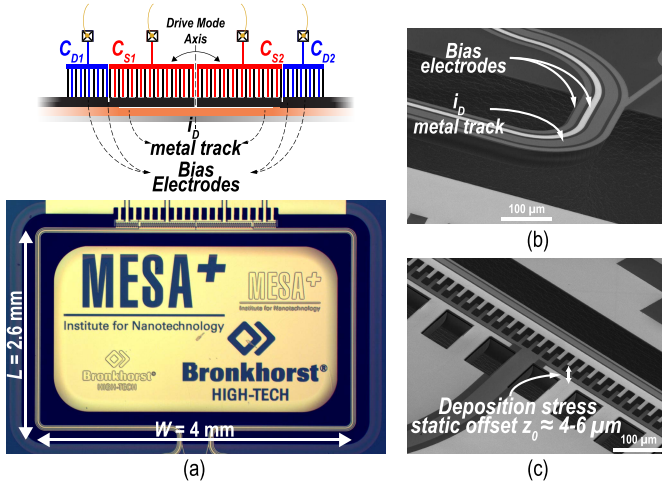


Fig. 2. (a) Micrograph of the SCT-fabricated MEMS Coriolis mass flow sensor and integrated readout capacitors illustration, (b) SEM images showing the access electrodes above the suspended channel, and (c) static offset  $z_0$  between the readout electrodes.

channel itself must be small compared with the mass of the fluid moving through it. Previous MEMS Coriolis designs used silicon to fabricate the sensor channel, leading to heavy, stiff, and low sensitivity sensors [11], [12]. Here, the sensor is fabricated using SiRN with a bulk-micromachining-based SCT process, as explained in detail in [25] and [26].

Fig. 2 shows the micrograph and scanning electron microscope (SEM) images of the fabricated rectangular shape device [15]. It consists of a suspended channel with a wall thickness ( $t_w$ ) of  $1.2 \mu\text{m}$  and an inner diameter ( $d_{in}$ ) of about  $60 \mu\text{m}$  [16]. The size of the channel [ $W \times L$ , in Fig. 2(a)] is limited by the need to keep  $m_{ch}$  small. In this work,  $W = 4 \text{ mm}$  and  $L = 2.6 \text{ mm}$ . This results in a ( $\omega_D/\omega_S$ ) ratio of about 1.75, which ensures that  $y_S$  is quite insensitive to variations in  $Q_S$ , since, from (3),  $y_S$  will change by less than 0.1% in response to a  $\pm 50\%$  variation in  $Q_S$ .

### C. Capacitive Readout

To read out the  $x_D$  and  $y_S$  displacements, capacitive electrodes with  $2.7\text{-}\mu\text{m}$ -thick comb fingers are integrated in the sensor, as shown in Figs. 1 and 2. Metal tracks are deposited on the top of the channel to access the electrodes and to provide a path for  $i_D$ , as shown in Fig. 2(b). The mechanical stress caused by these tracks creates a static offset ( $z_0$ ) between the comb electrodes [see Fig. 2(c)], which ensures that the resulting capacitance change ( $\Delta C$ ) is a monotonic function of displacement. Furthermore, this design simplifies the fabrication process and reduces squeezed film damping, which results in a drive mode quality factor  $Q_D > 60$  without vacuum encapsulation, thus allowing the sensor to operate at atmospheric pressure, unlike [12] and [22].

For large displacements, when the overlap between the electrodes tends to zero, the resulting  $\Delta C$  will become a nonlinear function of displacement. To mitigate this, the detection combs ( $C_{D1,2}$  and  $C_{S1,2}$ ) are symmetrically placed around the drive mode rotation axis. This placement limits the

TABLE I  
TYPICAL PARAMETERS OF THE MEMS CORIOLIS MASS FLOW SENSOR

Parameter	Value	Unit
Suspended Channel Size ( $W \times L$ )	$4 \times 2.6$	$\text{mm}^2$
Channel Mass ( $m_{ch}$ )	$\sim 15$	$\mu\text{g}$
Channel Diameter ( $d_{in}$ )	$< 60$	$\mu\text{m}$
Wall Thickness ( $t_w$ )	1.2	$\mu\text{m}$
Drive Resonance Frequency ( $f_D$ )	1.78 - 3	kHz
Sense Resonance Frequency ( $f_S$ )	1.01 - 1.71	kHz
Sense Mode Q-Factor ( $Q_S$ )	40	-
Drive Displacement ( $x_D$ )	10	$\mu\text{m}$
Drive Current ( $i_{DRIVE}$ )	5	mA
Readout Comb Offset ( $z_0$ )	4 - 6	$\mu\text{m}$
Sense DC Bias ( $V_{BS}$ )	20	V
Mass Flow Sensitivity* ( $\Delta C_S/\Phi$ )	[300 - 400]	aF/(g/h)
Brownian Noise**	$\sim 1$	$\mu\text{g/h}/\sqrt{\text{Hz}}$

\*Estimate from  $N_2$  to  $H_2O$ . \*\*[19]

maximum displacement experienced by the combs to less than  $z_0$  ( $\approx 4 \mu\text{m}$ ), thus ensuring adequate linearity in  $\Delta C$ .

For  $x_D$  detection, the differential motion around the drive mode should be sensed. Compared with the comb pair  $C_{S1,2}$ , the pair  $C_{D1,2}$  is more sensitive to  $x_D$ , since they are located further away from the drive rotation axis. So,  $C_{D1,2}$  are used to detect drive motion, while  $C_{S1,2}$  are used to detect sense motion. The  $C_{D1,2}$  and  $C_{S1,2}$  standoff capacitances are in the order of 25 and 45 fF and typically change by  $\pm 3$  and  $\pm 1$  fF each, respectively. Table I summarizes the typical values for the key mechanical parameters of the sensor used in this work.

### D. Mass Flow Sensing Readout

Although combs  $C_{S1,2}$  are intended to detect the sense motion, they still experience large changes due to  $x_D$  ( $\Delta C_X$ ) and only small changes due to  $y_S$  ( $\Delta C_Y$ ), as shown in Fig. 1. In the time domain, these capacitance changes are orthogonal to each other [see Fig. 1(c)], and so,  $C_{S1}$  and  $C_{S2}$  can be expressed as follows:

$$C_{S1} = \Delta C_Y \cos(\omega_D t) + \Delta C_X \sin(\omega_D t) \quad (4)$$

$$C_{S2} = \Delta C_Y \cos(\omega_D t) - \Delta C_X \sin(\omega_D t). \quad (5)$$

Consequently, the phase difference ( $\Delta\phi$ ) between  $C_{S1}$  and  $C_{S2}$  due to  $y_S$  can be expressed as follows [17]:

$$\Delta\phi = 2 \arctan\left(\frac{\Delta C_Y}{\Delta C_X}\right) \propto \Phi \quad (6)$$

where  $\tan(\Delta\phi) \approx \Delta\phi$  for small phase shifts. Therefore, mass flow ( $\Phi$ ) is directly proportional to the ratio  $\Delta C_Y/\Delta C_X$  and so is robust to variations in the amplitude of  $x_D$ .

The resulting readout architecture is shown in Fig. 3(a), where each comb  $C_{S1,2}$  is biased by a DC voltage ( $V_{BS}$ ) and then readout by a capacitance-to-voltage (C/V) converter and





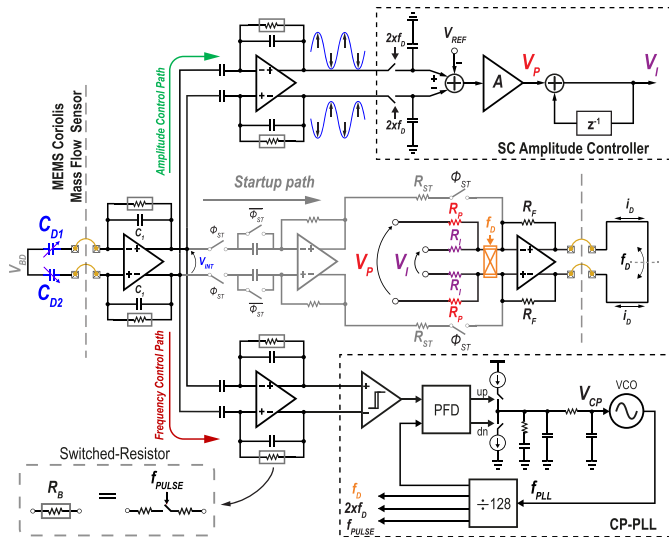


Fig. 5. Simplified circuit implementation of the drive loop showing the startup, frequency, and amplitude control paths.

packaging stress, and aging-related effects. To estimate  $\phi_{err}$  and compensate for the  $\Phi_Q$  residual drift, an additional demodulator is used to monitor the  $Q$  signal.

$V_{SENSE}$  is digitized with high resolution ( $> 14$  bits) by  $I$  and  $Q$  delta-sigma modulators ( $\Delta\Sigma$ Ms),  $I$ - $\Delta\Sigma$ M and  $Q$ - $\Delta\Sigma$ M, respectively. Their respective bitstream outputs,  $BS_I$  and  $BS_Q$ , are then decimated and combined with appropriate weights ( $k_0$ ) in the digital domain to cancel any residual  $Q$  error [28]. The estimation of  $\phi_{err}$  [ $\approx 90^\circ \pm \arctan(Q/I)$ ] is performed at zero flow in a temperature stable environment. The resulting  $k_0 \approx \pm\phi_{err}$  is then fixed and used for all subsequent measurements. It is important to note that any in-phase and quadrature parasitic couplings that appear at  $\Phi_I$  and  $\Phi_Q$  [29] may affect the accuracy of  $\phi_{err}$  estimation, thus leading to residual errors in the cancellation of  $\Phi_Q$  in (7).

### B. Drive Loop Circuit Implementation

The simplified circuit implementation of the drive loop is shown in Fig. 5. Differential changes in  $C_{D1,2}$  are converted into a voltage ( $V_{INT}$ ) by a low noise capacitive transimpedance amplifier (C-TIA). Its gain is set by a feedback capacitor  $C_1 = 1$  pF and varies from 154 to 158 dB $\Omega$ , as  $f_D$  varies from 1.8 kHz (liquids) to 3 kHz (gases). For the drive loop, the sensor can be simply seen as a resonator. Thus, as given by (7), the phase noise of the demodulating reference ( $f_D$ ) should be minimized to avoid increasing the mass flow noise floor. For a given drive mode  $Q$ -factor ( $Q_D$ ), this can be achieved by increasing  $V_{BD}$  and  $x_D$  and reducing the C-TIA's noise [35]. The former is set to 20 V and  $\sim 10$   $\mu$ m, respectively, to prevent the pull-in of the  $C_{D1,2}$  combs and to ensure that the resonator operates in its linear region. With this, the C-TIA's input referred current noise is designed to be  $< 12$  fA/ $\sqrt{\text{Hz}}$  over the  $f_D$  operating range.

To guarantee proper startup at  $f_D$ , the integrating C-TIA is followed by a differentiator during the startup phase ( $\phi_{ST}$ ). This adds an extra  $90^\circ$  phase shift to  $V_{INT}$  to ensure oscillation [36], while a driver with a gain  $R_F/R_{ST}$  provides the

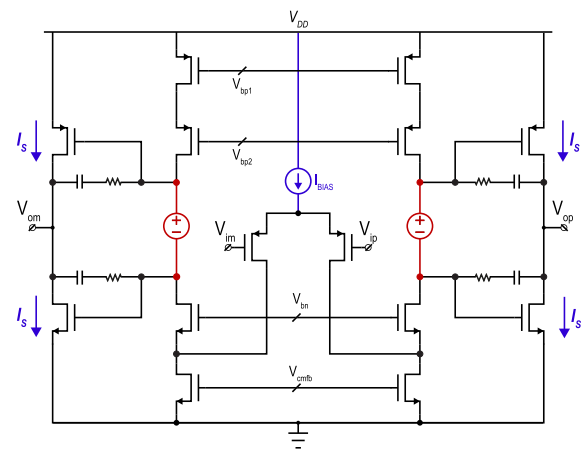


Fig. 6. Schematic of the two-stage op-amp used to implement the driver.

drive current  $i_D$ . Fig. 6 shows the two-stage op-amp used to implement the driver. It employs a class-AB output stage to efficiently provide the large currents ( $\approx 10$  mA) needed to drive the 175- $\Omega$  metal track with rail-to-rail ( $1.8V_p$ ) signals. A static current ( $I_s$ ) of 1 mA is enough to provide the peak  $i_D$ .

The clock signals used in the drive loop are provided by a charge-pump (CP) PLL. This is driven by a comparator with hysteresis, which converts  $V_{INT}$  into a well-defined square wave. Once the PLL locks to  $f_D$ , which takes place within 25 ms, the startup path is disabled, and the drive loop is controlled by the PLL's output. The comparator's hysteresis is also reduced to avoid phase errors [30]. Compared with conventional sustaining circuits [14], this PLL-based frequency control ensures robustness to the sensor's parasitic resonant modes and simplifies the generation of the drive loop and sense readout clocks [31]. During normal operation, the output of the C-TIA is boosted by two capacitively coupled amplifiers (CCAs), which drive the PLL and the amplitude regulator, respectively. They block the output offset of the C-TIA and isolate it from the kickback of the PLL's comparator and the amplitude controller's switching transients.

DC feedback around the C-TIA and CCAs is provided by G $\Omega$  bias resistors ( $R_B$ ) to ensure that the associated high-pass corner frequencies are at least two orders of magnitude lower than  $f_D$  (1.8–3 kHz). As a result, the associated phase shift has a negligible effect on drive loop operation. Although pseudo-resistors offer an area-efficient way to realize G $\Omega$  resistors, they require process/temperature compensation to ensure reliable operation [37]. In this work, switched resistors [38], [39] are used to boost 1-M $\Omega$  poly resistors to  $> 5$  G $\Omega$ . As shown in Fig. 5, the PLL provides the duty-cycled clock signal  $f_{PULSE} (= 16 \times f_D)$  to realize  $R_B$ .

In the amplitude control path (see Fig. 5), a switched-capacitor (SC) network provides amplitude regulation by sampling the peak of  $V_{INT}$  synchronously [30], [32] and comparing it with a reference voltage ( $V_{REF}$ ). The  $Q$ -factor of the sensor's drive mode ( $Q_D$ ) is quite limited ( $\sim 60$ – $\sim 100$ ). Thus, a proportional-integral (PI) controller is used to achieve accurate control of the drive amplitude. To decouple the controller parameters, the proportional and

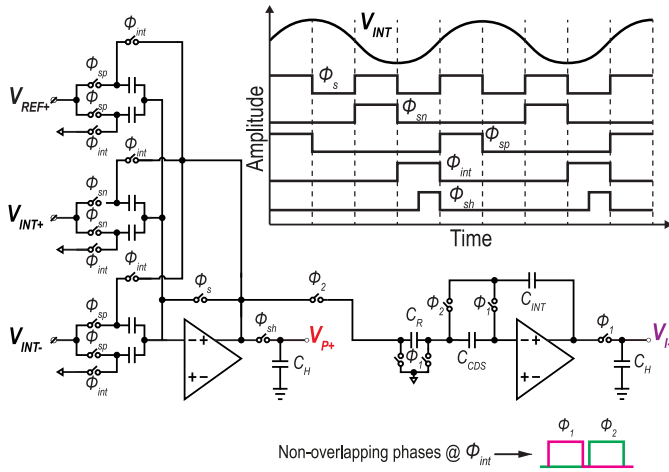


Fig. 7. Half circuit of the SC amplitude controller.

integral gains are set by resistors  $R_P$  and  $R_I$ , respectively. These convert the proportional ( $V_P$ ) and integral ( $V_I$ ) voltages into currents, which are then up-modulated to  $f_D$  and summed at the driver's virtual ground, thus providing the amplitude-controlled  $i_D$  at a steady state.

Since  $\Delta C_S$  is modulated by  $f_D$  and is proportional to  $x_D$ , amplitude control signals with low  $1/f$  noise are required for good long-term stability [14], [33], [40]. Fig. 7 shows the simplified half circuit of the SC amplitude controller and its timing diagram. It consists of a flip-around amplitude detector [34], which generates the controller's error voltage by detecting the amplitude of  $V_{INT}$  and comparing it with  $V_{REF}$ . It is followed by a correlated-double-sampling (CDS) SC integrator, which samples and integrates the error voltage.  $V_P$  and  $V_I$  are sampled and held by large  $C_H$  ( $\approx 10$  pF) capacitors, which are buffered before being fed to  $R_P$  and  $R_I$ . Since both positive and negative peaks of  $V_{INT}$  are compared, the offset of the preceding stages is cancelled. This leads to a low  $1/f$  noise, stable, and offset-free control of the drive amplitude.

The sensor is used for liquids and gases, and therefore, the drive loop must be able to operate with a wide range of resonance frequencies while at the same time accommodating changes in  $Q_D$ . Due to the SC implementation, most of the controller's time constants are locked to  $f_D$ . Therefore, the drive loop remains stable with both liquids and gases.

### C. Sense Front-End Implementation

Fig. 8(a) shows the circuit implementation of the sense C/V front-end. It consists of a low-noise C-TIA that converts  $\Delta C_S$  into a voltage  $V_{SENSE}$ , which contains mass flow information at  $f_D$ . Around  $f_D$ , its input-referred current noise can be expressed as follows [36]:

$$i_{n,i}^2 = v_{n,OTA}^2 [(C_S + C_F + C_P + C_{GG})s]^2 + i_{n,B}^2 \quad (8)$$

where  $v_{n,OTA}^2$  is the input-referred voltage noise of the OTA used to implement the C-TIA,  $i_{n,B}^2 = 4kT/R_B$  is the feedback resistor equivalent current noise,  $k$  is Boltzmann's constant,  $T$  is the temperature, and  $C_F$ ,  $C_P$ , and  $C_{GG}$  are the feedback,

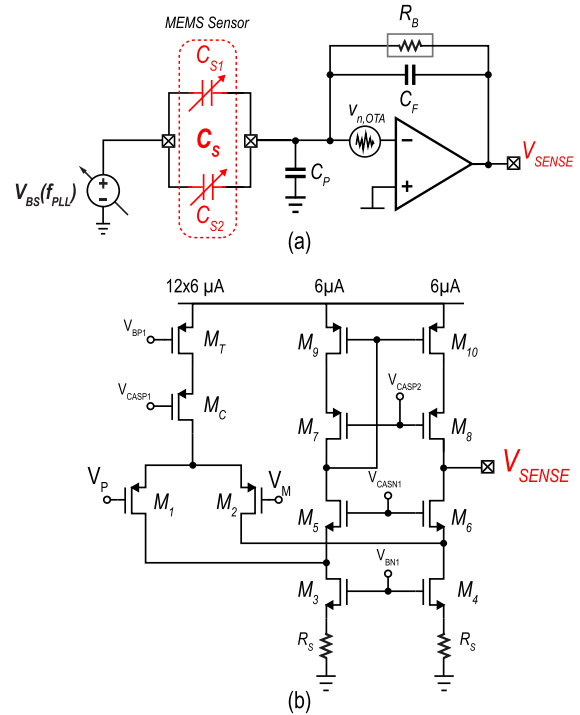


Fig. 8. (a) Sense readout capacitors C-TIA front end and (b) its OTA implementation.

the parasitic, and the OTA's input capacitances, respectively. As in the drive loop C-TIA, the large DC feedback resistor  $R_B$  ( $> 5$  G $\Omega$ ) is realized by a switched resistor. As a result, the sense C-TIA input-referred noise is mainly determined by the OTA's voltage noise in combination with the total input capacitance.

The schematic of the OTA used in the sense C-TIA is shown in Fig. 8(b). When operated with  $H_2O$ ,  $f_D \approx 1.8$  kHz, and so, the OTA's  $1/f$  corner frequency must be lower than this. A folded-cascode topology provides  $> 85$ -dB DC gain, which is enough to establish a well-defined virtual ground for the biasing of the sense combs. To achieve low  $1/f$  noise, the input pair ( $M_1$ – $M_2$ ) consist of large (1000/0.6  $\mu m$ ) transistors. They are sized, such that their input capacitance ( $C_{GG}$ ) is less than 1/3 of the total parasitic capacitance ( $C_P > 10$  pF) at the virtual ground, thus limiting their contribution to the total noise in (8). The OTA's current sources ( $M_3$ – $M_4$ ) are degenerated by resistors  $R_S$ , which reduces their  $1/f$  noise at the expense of thermal noise. To mitigate this, a 1/12 current ratio is used between the input-pair tail ( $M_T$ ) and the current sources ( $M_9$ – $M_{10}$ ) in the folding branch, thus reducing their transconductance and, hence, their  $1/f$  noise. This leads to a  $1/f$  corner frequency of  $\sim 1.5$  kHz.

### D. IQ- $\Delta\Sigma$ Ms Implementation

Fig. 9 shows the simplified circuit diagram of the I- $\Delta\Sigma$ M used in the sense readout channel. It is based on the second-order CT- $\Delta\Sigma$ M. The sensed  $V_{SENSE}$  containing mass flow information at  $f_D$  (node I) is converted into a current by the first integrator's input resistor ( $R_{IN}$ ). The resulting current is then demodulated to DC by a passive mixer (chopper)



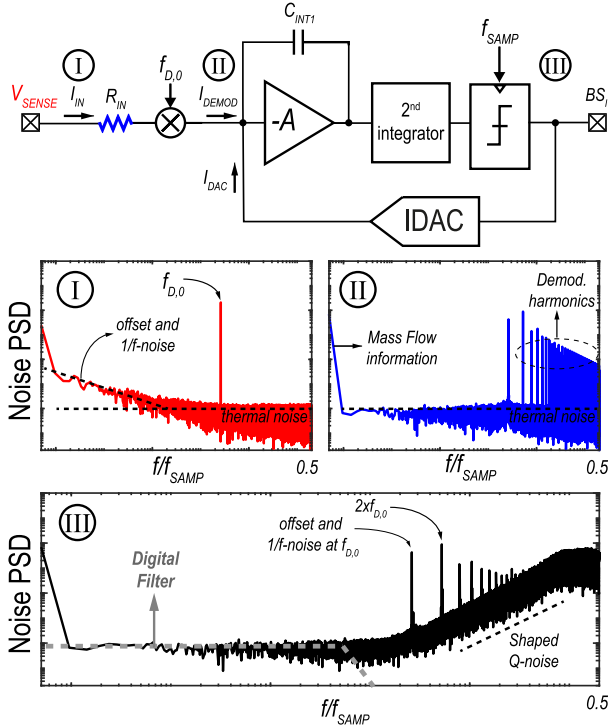


Fig. 9. Simplified circuit diagram of the sense readout  $I$ - $\Delta\Sigma$ M and its noise PSD.

with a reference  $f_{D,0}$ , which is in-phase with the mass flow component in  $V_{\text{SENSE}}$ . Then, the downconverted current ( $I_{\text{DEMOD}}$ ) is the input of  $\Delta\Sigma$ M (node II). As a result, the modulator's bitstream ( $BS_I$ ) average is, thus, a measure of mass flow ( $\Phi$ ). The offset and  $1/f$  noise components in  $V_{\text{SENSE}}$  will be modulated to the harmonics of  $f_{D,0}$ , where they are removed by the modulator's digital decimation filter (node III).

Since the symmetrical placement of  $C_S$  around the drive mode axis inherently attenuates the amount of  $Q$  error in  $V_{\text{SENSE}}$ , the extra harmonics caused by the residual  $Q$  error can also be removed by the decimation filter. As discussed in Section III-A, an additional  $Q$ - $\Delta\Sigma$ M is used to compensate for the residual drift in  $BS_I$  due to  $Q$  as well as to estimate  $\varphi_{\text{err}}$ .

Fig. 10 shows the schematics of the sense readout used in the  $\Phi$ DC. The sense C-TIA output is boosted by a CCA, which functions as a single-to-differential stage that drives both  $I$ - and  $Q$ - $\Delta\Sigma$ Ms [see Fig. 10(a)]. The  $I/Q$  passive mixers are implemented by NMOS choppers placed between the  $\Delta\Sigma$ M first integrator's virtual ground and the input resistor ( $R_{\text{IN}}$ ), as shown in Fig. 10(b) [41]. Thus, high linearity can be achieved, since the voltage swing across the chopper's nonlinear switches is only a fraction of the input signal swing. Since a square wave is used for demodulation, odd harmonics will be demodulated back to DC with the wanted signal, with the third-order harmonic being the most dominant among them. The third-harmonic distortion ( $HD_3$ ) of the mixers can be approximated as follows [42]:

$$HD_3 = \frac{3}{32} \left( \frac{V_{\text{IN}}}{V_{\text{GT}}} \right)^2 \cdot \left( \frac{r_{\text{ON}}}{R_{\text{IN}}} \right)^3 \quad (9)$$

where  $V_{\text{GT}}$  is the gate overdrive voltage, and  $V_{\text{IN}}$  is the maximum demodulator input. To keep  $HD_3 < -130$  dB,

the switch resistance  $r_{\text{ON}}$  ( $\approx 1.5$  k $\Omega$ ) is much smaller than  $R_{\text{IN}}$  (180 k $\Omega$ ).

The downconverted  $I/Q$  currents, and their harmonics, provided by the CCA are digitized by two second-order CT- $\Delta\Sigma$ Ms using feedforward (FF) loop filters with finite impulse response (FIR) DAC [43], as shown in Fig. 10(a). The use of four-tap FIR-DAC reduces the swing of current error to be processed by the first integrator, thus improving the passive mixer's linearity. Furthermore, for the sampling frequency ( $f_{\text{SAMP}}$ ) of 500 kHz, the use of a FIR-DAC allows the first integrator to be chopped at a fraction of  $f_{\text{SAMP}}$  ( $1/8$ ), mitigating its offset and  $1/f$  noise without incurring quantization noise folding [44]. The first stage amplifier is a two-stage miller-compensated op-amp based on current-reuse stages [see Fig. 10(c)]. Its energy-efficient design allows the two  $\Delta\Sigma$ Ms to consume about 200  $\mu$ W, thus adding little to the overall system power consumption. The second integrator is implemented in an FF fashion, which also facilitates the use of a capacitive DAC (CDAC) to compensate for the delay added by the main FIR-DAC.

The resulting bitstreams ( $BS_I$  and  $BS_Q$ ) are decimated off-chip and then recombined to realize the low-drift mass flow digital output of the  $\Phi$ DC. Moreover, since the offset of the stage preceding the  $\Delta\Sigma$ Ms is up-modulated to  $f_D$ , and the first integrator is chopped, the ratio between  $BS_I$  and  $BS_Q$  averages ( $\mu_Q/\mu_I$ ) at zero flow can be used as a measure of  $\varphi_{\text{err}} \approx 90^\circ \pm \arctan(\mu_Q/\mu_I)$  with negligible error.

#### IV. MEASUREMENT RESULTS

The integrated CMOS sensor interface [see Fig. 11(a)] was implemented in a standard 0.18- $\mu$ m process and co-integrated with the SCT-fabricated MEMS Coriolis mass flow sensor in a chip-on-board assembly for prototype testing [see Fig. 11(b)]. The interface circuitry and the MEMS chip occupy  $2.2 \times 2.2$  and  $15 \times 7.5$  mm, respectively. For flexibility and testability, the required digital logic and HV bias generation were implemented off-chip. The complete system draws about 7.2 mA from a 1.8-V supply during steady-state operation.

A daughter printed-circuit board (PCB) containing the  $\Phi$ DC is mounted over a small custom 3D printed fluid connector. To prevent leakage, O-rings are used below the PCB. At the same time, a metal clamp containing the magnets to generate  $B \approx 50$  mT tightens the fluidic connection. This is possible, since the MEMS samples include glass caps that are integrated into the sensor at the wafer level.

The fluid connector and the setup used for mass flow measurements are shown in Fig. 11(c). Several fluids, from liquids to gases, are used for the characterization of the proposed system: nitrogen ( $N_2$ ), argon (Ar), carbon dioxide ( $CO_2$ ), water ( $H_2O$ ), isopropanol (IPA), and mixtures of  $H_2O + IPA$ . Pressure regulated (6 bar) tanks are used for gases and pressurized (2 bar) Falcon tubes for liquids. Bronkhorst mini Cori-FLOW mass flow controller and sensor are used at the flow input and output, respectively, and serve as a reference [21]. This way, the mass flow through the device under test can be guaranteed with negligible leakage. The daughter PCB is connected below a motherboard, and a flat cable is used to communicate with

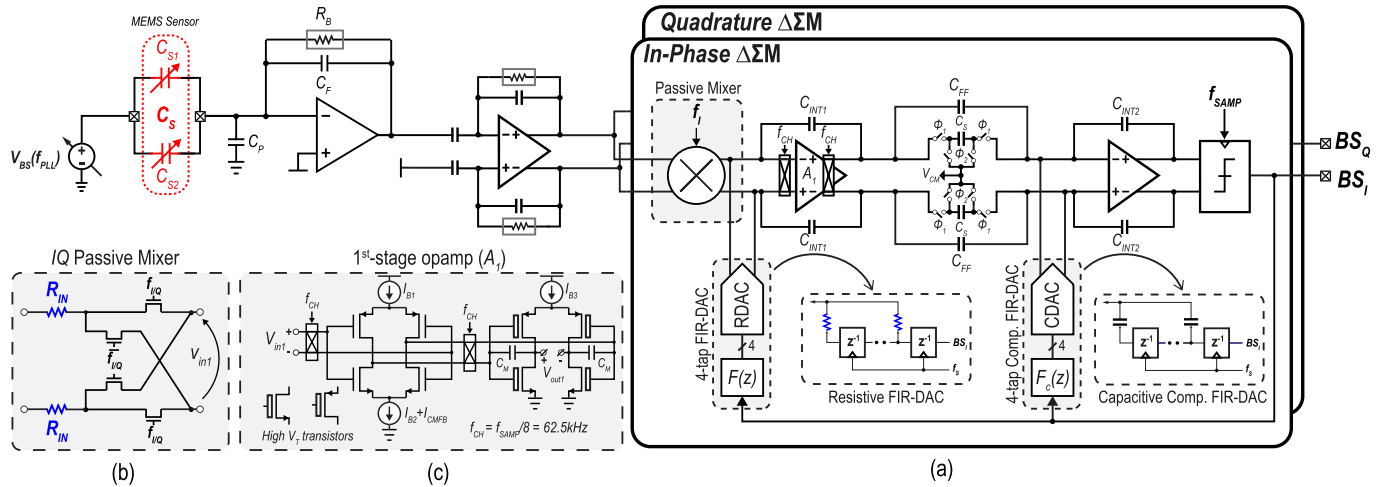


Fig. 10. Detailed schematic of the (a) proposed  $\Phi$ DC, (b) passive mixer, and (c) first integrator opamp implementation.

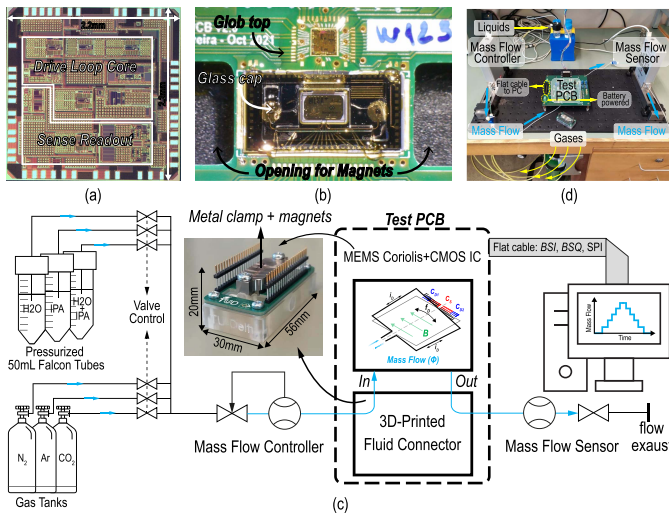


Fig. 11. (a) Micrograph of the fabricated 0.18- $\mu\text{m}$  CMOS sensor interface. (b) Chip-on-board co-integration with the SCT-fabricated MEMS Coriolis mass flow sensor. (c) Mass flow measurement setup illustration, 3D printed fluid connector close-up, and (d) photograph of the actual setup.

a PC to acquire the ADCs bitstreams and define the system's setting via SPI. The complete setup is shown in Fig. 11(d).

Fig. 12 shows the  $\Phi$ DC decimated output for mass flows of liquids and gases up to 5 and 2 g/h, respectively, with 250 mg/h, for a fixed  $V_{BS} = 20\text{ V}$ . The outputs of both increasing and decreasing mass flow are overlapped, thus showing that the sensor has no hysteresis. Since the  $\Delta\Sigma$ s have to process the mass flow signal at DC, its harmonics, and the up-modulated front-end offset, the flow range is limited to 5 g/h to avoid saturating the modulators.

The sensor's mass flow sensitivity has a linear relationship with  $f_D$ , as shown by the red dashed line in Fig. 13(a), which is expected from (3). To achieve a single response from liquids to gases, a resonance frequency-dependent gain calibration can be performed in the digital domain [14]. However, this leads to fluid-dependent resolution, since both noise and signal are scaled simultaneously. Here, a relatively straightforward background sensitivity tuning (BST) scheme

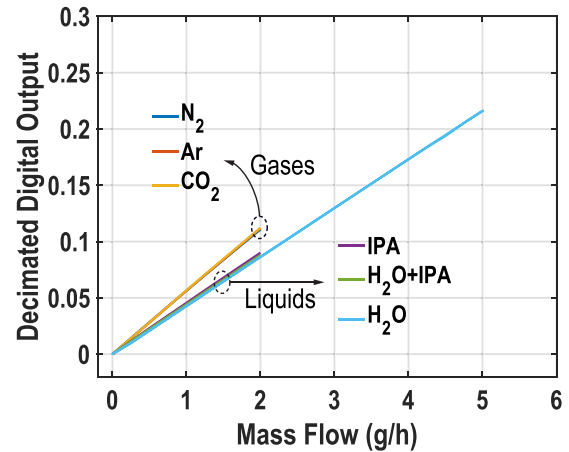
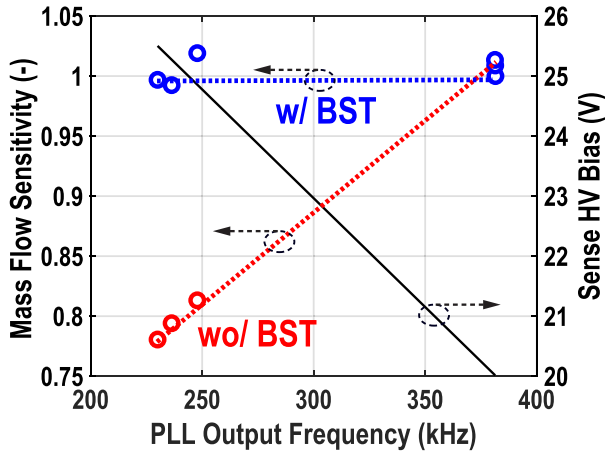


Fig. 12. Measured  $\Phi$ DC decimated output versus mass flow for liquids and gases.

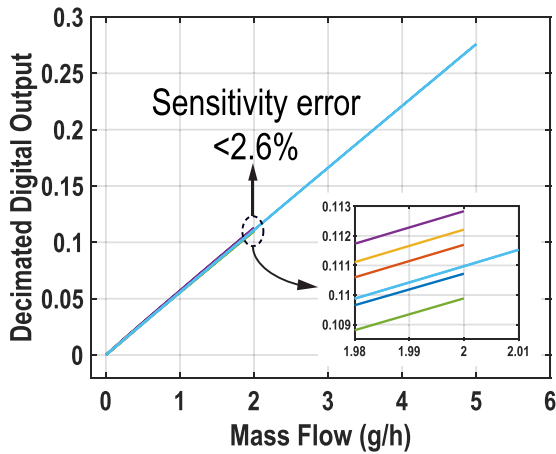
performs a frequency-dependent gain calibration in the analog domain. This calibration scheme is described as follows.

- 1) Sensitivities at  $N_2$  and  $H_2O$  are matched: Having the highest sensitivity as a reference ( $N_2$  with  $V_{BS} = 20\text{ V}$ ),  $V_{BS}$  for  $H_2O$  is increased until its sensitivity matches that of  $N_2$  at 2 g/h [see Fig. 13(a)].
- 2) Relationship Between  $f_D$  and  $V_{BS}$ : From step 1), a linear fit between  $N_2$  and  $H_2O$  is obtained to map the required  $f_D$  to  $V_{BS}$  relationship to match their sensitivities [see Fig. 13(a) (black solid line)].
- 3) Based on 1) and 2),  $V_{BS}$ , when operating with all fluids between  $N_2$  and  $H_2O$ , is tuned continuously in the background proportionally to  $f_D$ .

The normalized sensitivities with and without the BST scheme are shown in Fig. 13(a). The  $\Phi$ DC mass flow response after the calibration is performed, and  $V_{BS}$  is tuned externally in the background, is shown in Fig. 13(b), with a between fluids sensitivity error of  $<2.6\%$ . Although most of the sensitivity drop is compensated by the increase in  $V_{BS}$ , the relatively large residual error indicates that changes in  $(\omega_D/\omega_S)$  due to pressure drop or compressibility [18], and variations in drive amplitude and capacitive readout nonlinearity related



(a)



(b)

Fig. 13. (a) Normalized mass flow sensitivity versus resonance frequency. (b) Mass flow response after BST.

effects, which are not proportional to  $f_D$ , might also have to be compensated to obtain lower sensitivity errors. Moreover, the expected flow error at 2 g/h for the used reference flow sensor [21] is expected to be about  $\pm 1\%$ .

Coriolis sensors are often required to achieve mass flow errors in the order of  $\pm 0.5\%$  [24]. To achieve this, up to ten mass flow points are often used to fit the sensor's response. The  $\Phi$ DC relative mass flow error is shown in Fig. 14. Its output is fit by the fifth-order polynomial and compared with the actual mass flow. Its errors are well within the "trumpet curve" boundaries, representing the ZS of the reference sensor ( $ZS_{REF}$ ) plus its  $\pm 0.5\%$  calibrated error. The error is relatively similar for liquids and gases and stays below  $\pm 1\%$  at 250 mg/h.

The bitstream spectra ( $\sim 33.5$ -s interval, Hanning window,  $16\times$  averaging) of  $\Phi$ DC output under zero flow condition for when the sensor is filled with  $N_2$  and  $H_2O$  are shown in Fig. 15. It shows a noise floor of about  $80 \mu\text{g/h}/\sqrt{\text{Hz}}$  after compensating for the drop in sensitivity when operating with  $H_2O$ . The up-modulated offset and the demodulation harmonics are filtered by a  $\text{sinc}^2$  decimation filter. With the parameters in Table I, this indicates that the equivalent capacitance resolution is below  $24 \text{ zF}/\sqrt{\text{Hz}}$ , which is mainly limited by thermal noise of the sense C/V converter.

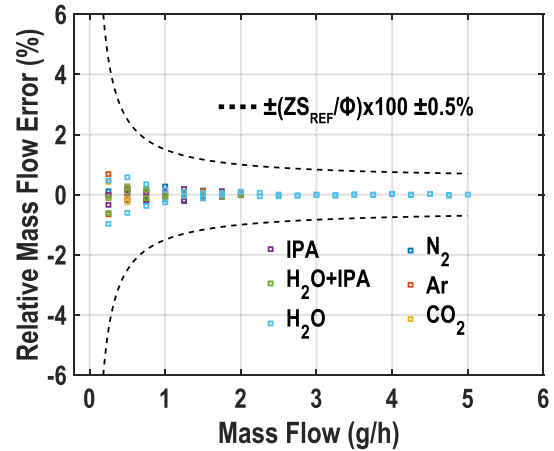
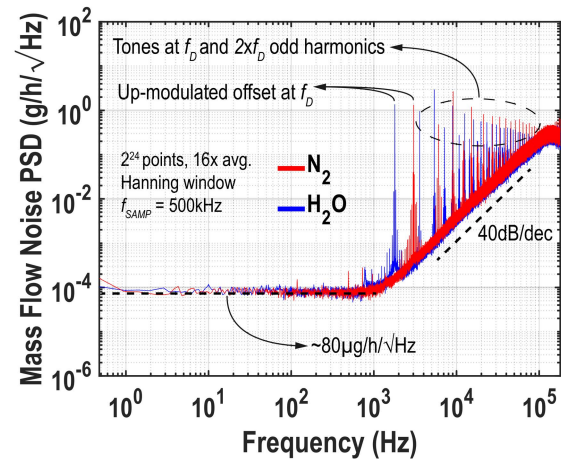


Fig. 14. Relative mass flow error for all tested fluids after the fifth-order polynomial fit.


 Fig. 15. Mass flow noise power spectral densities for  $N_2$  and  $H_2O$ .

To obtain the ZS of the sensor, its decimated output in a 4-Hz bandwidth was observed at zero flow, when filled with  $H_2O$ , and room temperature. As shown in Fig. 16, it achieves a  $\pm 0.31 \text{ mg/h}$  standard deviation for a measurement time of about 4 h and is relatively constant with both  $N_2$  and  $H_2O$  [15].

The combined phase error ( $\varphi_{err}$ ) due to the sense mode limited  $Q$ -factor and C/V front-end causes the output to drift, since  $Q$  leaks into the wanted mass flow signal ( $I$ ). Fig. 17 shows the Allan deviation for the data in Fig. 16. Its minima ( $\sim 8 \mu\text{g/h}$ ), which represents the lowest resolution achievable by averaging, is limited by  $1/f$  noise. The minima is improved by about  $1.6\times$  when the compensation is used. This indicates that  $Q$ , and thus its induced drift, is already substantially reduced by design, since the sense combs experience much smaller displacements than the actual  $x_D$ . Moreover, the minima is  $19\times$  smaller than that obtained with conventional phase readout [14], thus showing how the use of a single C/V converter to readout  $C_S = C_{S1} + C_{S2}$  minimizes the drift due to the large  $Q$  signal while at the same time reducing the noise floor by more than 3 dB.

TABLE II  
PERFORMANCE SUMMARY AND COMPARISON

	[8]	[9]	[10]	[21]	[12]	[13]	[14]	This Work
Sensor Type	MEMS Thermal	MEMS Thermal	MEMS Thermal	SS Coriolis	MEMS Coriolis	MEMS Coriolis	MEMS Coriolis	MEMS Coriolis
Readout Technology	CMOS	0.18 $\mu$ m CMOS	COTS	COTS	COTS	COTS	0.18 $\mu$ m CMOS	0.18 $\mu$ m CMOS
ASIC Output	Analog	Analog	Analog	-	-	Analog	Analog	Digital
Fluids	H <sub>2</sub> O	N <sub>2</sub>	N <sub>2</sub>	Liquids & Gases	Liquids (H <sub>2</sub> O/IPA)	N <sub>2</sub>	Liquids & Gases	Liquids & Gases
Full Scale (g/h)	0.09	0.36 <sup>c</sup>	0.09 <sup>c</sup>	5	500	0.75	5	5
Noise Floor ( $\mu$ g/h/ $\sqrt{\text{Hz}}$ )	<600 <sup>a</sup>	<200	<100	<4000 <sup>a</sup>	N/A	NA	300	80
Bandwidth (Hz)	4	25	25	3	1.6	0.63	3	4
Dynamic Range <sup>b</sup> (dB)	43.5	65.1	59	61.9	N/A	N/A	84.4	95.9
Zero Stability (mg/h)	N/A	N/A	N/A	$\pm 10$	$\pm 223$	2.6	$\pm 0.8$	$\pm 0.31$
Power Consumption (mW)	21.5	8.9	13.1	2500	400	1250	14.6	13

<sup>a</sup>Estimated from repeatability. <sup>b</sup>1Hz bandwidth. <sup>c</sup>Limited to the linear range. N/A = Specification not available

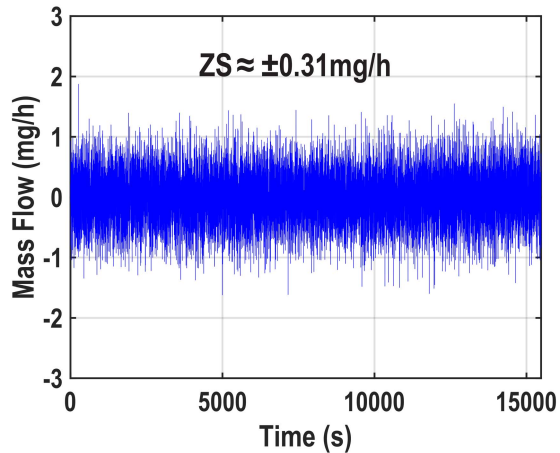


Fig. 16. Measured zero stability when the sensor is filled with H<sub>2</sub>O.

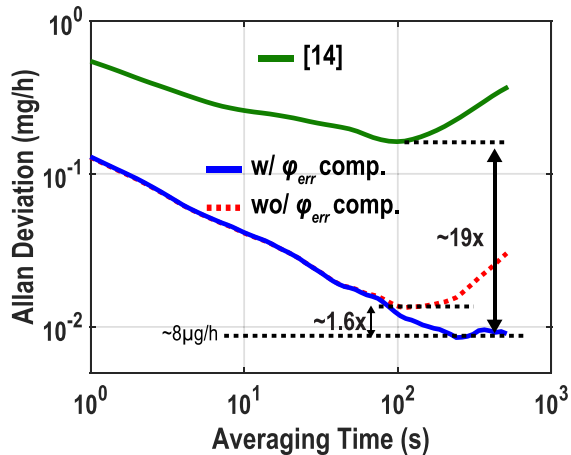


Fig. 17. Allan deviation of the mass flow output with and without phase-error compensation and its comparison with [14].

An advantage of MEMS Coriolis mass flow sensor over other sensing principles is its ability to estimate fluid density [23]. To measure this, the sensor is filled with different

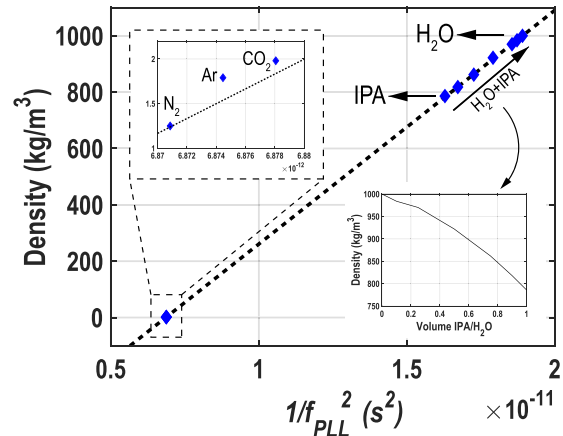


Fig. 18. Measured density to resonance frequency relationship.

fluids, and its resonance frequency change is observed with a frequency counter (Keysight 53230A). The relationship between fluid density and resonance frequency is measured under ambient pressure and zero flow. The sensor's measured density to  $f_D$  response is shown in Fig. 18. To cover the wide density range between H<sub>2</sub>O and IPA, the response for various mixtures of the two with volume ratios of 10/90, 25/75, 50/50, 75/25, and 90/10 is also included. As shown by the first-order fit dashed line, the response is a linear function of  $f_D^{-2}$ , where  $f_D = f_{PLL}/128$ , thus matching the expected response from (1). This relationship is more closely followed by liquids, since with gases, the added fluid mass ( $m_f$ ) is smaller than that of the suspended channel ( $m_{ch}$ ).

Table II summarizes the performance of the proposed  $\Phi$ DC and compares it with state-of-the-art MEMS Coriolis and MEMS thermal flow sensors. Compared with the lowest flow range miniaturized SS Coriolis sensor in the market [21], it achieves a  $>30\times$  improvement in resolution and ZS while dissipating  $>190\times$  less power.

Against MEMS Coriolis's prior works [13], [14], the proposed system provides a digital output, and its noise floor



and ZS are  $3.75\times$  and  $2.6\times$  lower, respectively, while remaining the same for all tested fluids. Furthermore, its performance is at par with state-of-the-art MEMS thermal flow sensors and, in some cases, even outperforms them [8].

## V. CONCLUSION

A  $\Phi$ DC capable of sensing low flow rates of liquids and gases, as well as their densities, has been presented. The system consists of a micromachined Coriolis flow sensor and a  $0.18\text{-}\mu\text{m}$  CMOS readout interface, which drives the sensor into resonance and digitizes the mass flow information. With the help of dynamic offset cancellation techniques applied to both drive and sense readout circuitry, low noise floor and low offset drift could be achieved. Similar performance for both liquids and gases is achieved using a resonance frequency-dependent sensitivity tuning scheme. Furthermore, the phase error in the sense readout path is cancelled in the digital domain, reducing quadrature-induced drift and improving its long-term stability. These advances lead to a MEMS Coriolis digital-output system with a state-of-the-art noise floor of about  $80\ \mu\text{g}/\text{h}/\sqrt{\text{Hz}}$  and a ZS of  $\pm 0.31\ \text{mg}/\text{h}$ . The proposed sensor is a promising alternative to MEMS thermal flow sensors in microfluidic and low-flow industrial applications, such as high-pressure liquid chromatography, drug infusion, and etching machines.

## REFERENCES

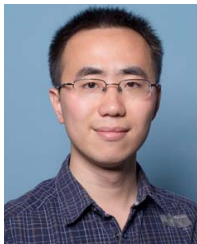
- [1] P. Murali, A. M. Niknejad, and B. E. Boser, "CMOS microflow cytometer for magnetic label detection and classification," *IEEE J. Solid-State Circuits*, vol. 52, no. 2, pp. 543–555, Feb. 2017.
- [2] K.-M. Lei et al., "A handheld high-sensitivity micro-NMR CMOS platform with B-field stabilization for multi-type biological/chemical assays," *IEEE J. Solid-State Circuits*, vol. 52, no. 1, pp. 284–297, Jan. 2017.
- [3] C. Hagleitner, D. Lange, A. Hierlemann, O. Brand, and H. Baltes, "CMOS single-chip gas detection system comprising capacitive, calorimetric and mass-sensitive microsensors," *IEEE J. Solid-State Circuits*, vol. 37, no. 12, pp. 1867–1878, Dec. 2002.
- [4] T.-H. Tzeng et al., "A portable micro gas chromatography system for lung cancer associated volatile organic compound detection," *IEEE J. Solid-State Circuits*, vol. 51, no. 1, pp. 259–272, Jan. 2016.
- [5] N. Nguyen, "Micromachined flow sensors—A review," *Flow Meas. Instrum.*, vol. 8, no. 1, pp. 7–16, 1997.
- [6] J. T. W. Kuo, L. Yu, and E. Meng, "Micromachined thermal flow sensors—A review," *Micromachines*, vol. 3, no. 3, pp. 550–573, 2012.
- [7] K. Makinwa and J. Huijsing, "A smart CMOS wind sensor," in *IEEE Int. Solid-State Circuits Conf. (ISSCC) Dig. Tech. Papers*, vol. 1, 2002, pp. 432–479.
- [8] *SLG-0025 Liquid Flow Meter Datasheet*, Sensirion AG, Stäfa, Switzerland, Mar. 2019.
- [9] M. Ahmed, W. Xu, S. Mohamad, F. Boussaid, Y.-K. Lee, and A. Bermak, "Fully integrated bidirectional CMOS-MEMS flow sensor with low power pulse operation," *IEEE Sensors J.*, vol. 19, no. 9, pp. 3415–3424, May 2019.
- [10] W. Xu, X. Wang, X. Zhao, Z. Ke, and Y.-K. Lee, "An integrated CMOS MEMS gas flow sensor with detection limit towards micrometer per second," in *Proc. IEEE 33rd Int. Conf. Micro Electro Mech. Syst. (MEMS)*, Jan. 2020, pp. 200–203.
- [11] P. Enoksson, G. Stemme, and E. Stemme, "A silicon resonant sensor structure for Coriolis mass-flow measurements," *J. Microelectromech. Syst.*, vol. 6, no. 2, pp. 119–125, Jun. 1997.
- [12] R. Smith, D. R. Sparks, D. Riley, and N. Najafi, "A MEMS-based Coriolis mass flow sensor for industrial applications," *IEEE Trans. Ind. Electron.*, vol. 56, no. 4, pp. 1066–1071, Apr. 2009.
- [13] A. C. de Oliveira, T. V. P. Schut, J. Groenesteijn, Q. Fan, R. J. Wiegerink, and K. A. A. Makinwa, "A MEMS Coriolis mass flow sensing system with combined drive and sense interface," in *Proc. IEEE SENSORS*, Oct. 2019, pp. 1–4.
- [14] A. C. de Oliveira, J. Groenesteijn, R. J. Wiegerink, and K. A. A. Makinwa, "A MEMS Coriolis mass flow sensor with  $300\ \mu\text{g}/\text{h}/\sqrt{\text{Hz}}$  resolution and  $\pm 0.8\ \text{mg}/\text{h}$  zero stability," in *IEEE Int. Solid-State Circuits Conf. (ISSCC) Dig. Tech. Papers*, vol. 64, 2021, pp. 84–86.
- [15] A. C. de Oliveira, S. Pan, and K. A. A. Makinwa, "A MEMS Coriolis-based mass-flow-to-digital converter with  $100\ \mu\text{g}/\text{h}/\sqrt{\text{Hz}}$  noise floor and zero stability of  $\pm 0.35\ \text{mg}/\text{h}$ ," in *IEEE Int. Solid-State Circuits Conf. (ISSCC) Dig. Tech. Papers*, vol. 65, 2022, pp. 1–3.
- [16] J. Haneveld et al., "Modeling, design, fabrication and characterization of a micro Coriolis mass flow sensor," *J. Micromech. Microeng.*, vol. 20, no. 12, 2010, Art. no. 125001.
- [17] D. Alveringh, R. J. Wiegerink, and J. C. Lötters, "Integrated pressure sensing using capacitive Coriolis mass flow sensors," *J. Microelectromech. Syst.*, vol. 26, no. 3, pp. 653–661, 2017.
- [18] Y. Zeng et al., "Design, fabrication, and characterization of a micro Coriolis mass flow sensor driven by PZT thin film actuators," *J. Microelectromech. Syst.*, vol. 30, no. 6, pp. 885–896, 2021.
- [19] D. Alveringh, R. J. Wiegerink, J. Groenesteijn, R. G. P. Sanders, and J. C. Lötters, "Experimental analysis of thermomechanical noise in micro Coriolis mass flow sensors," *Sens. Actuators A, Phys.*, vol. 271, pp. 212–216, Mar. 2018.
- [20] L. G. Pagani et al., "The first three-dimensional printed and wet-metallized Coriolis mass flowmeter," *IEEE Sensors Lett.*, vol. 4, no. 6, pp. 1–4, Jun. 2020.
- [21] *Mini CORI-FLOW Series ML120 Coriolis Mass Flow Meter Datasheet*, Bronkhorst BV, Ruurlo, Netherlands, Nov. 2019.
- [22] *MEMS Coriolis Nanomass Density Meter Datasheet*, TrueDyne Sensors AG, Reinach, Switzerland, Mar. 2017.
- [23] M. Yariesbouei, R. G. Sanders, T. Moazzenzade, R. J. Wiegerink, and J. C. Lötters, "Free suspended thin-walled nickel electroplated tubes for microfluidic density and mass flow sensors," *J. Microelectromech. Syst.*, vol. 31, no. 3, pp. 408–414, 2022.
- [24] T. Wang and R. Baker, "Coriolis flowmeters: A review of developments over the past 20 years, and an assessment of the state of the art and likely future directions," *Flow Meas. Instrum.*, vol. 40, pp. 99–123, Dec. 2014.
- [25] J. Groenesteijn et al., "A versatile technology platform for microfluidic handling systems, Part I: Fabrication and functionalization," *Microfluidics Nanofluidics*, vol. 21, pp. 1–14, Jul. 2017.
- [26] J. Groenesteijn, M. J. de Boer, J. C. Lötters, and R. J. Wiegerink, "A versatile technology platform for microfluidic handling systems, Part II: Channel design and technology," *Microfluidics Nanofluidics*, vol. 21, pp. 1–12, Jul. 2017.
- [27] M. Lutz et al., "A precision yaw rate sensor in silicon micromachining," in *Proc. Int. Solid State Sensors Actuators Conf.*, vol. 2, 1997, pp. 847–850.
- [28] C. D. Ezekwe, W. Geiger, and T. Ohms, "A 3-axis open-loop gyroscope with demodulation phase error correction," in *IEEE Int. Solid-State Circuits Conf. (ISSCC) Dig. Tech. Papers*, Feb. 2015, pp. 1–3.
- [29] L. G. Pagani et al., "Direct phase measurement and compensation to enhance MEMS gyroscopes stability," *J. Microelectromech. Syst.*, vol. 30, no. 5, pp. 703–711, 2021.
- [30] S. Rombach et al., "An interface ASIC for MEMS vibratory gyroscopes with a power of 1.6 mW, 92 dB DR and  $0.007^\circ/\text{s}/\sqrt{\text{Hz}}$  noise floor over a 40 Hz band," *IEEE J. Solid-State Circuits*, vol. 51, no. 8, pp. 1915–1927, Aug. 2016.
- [31] G. K. Balachandran, V. P. Petkov, T. Mayer, and T. Balslink, "A 3-axis gyroscope for electronic stability control with continuous self-test," *IEEE J. Solid-State Circuits*, vol. 51, no. 1, pp. 177–186, Jan. 2016.
- [32] M. Marx et al., "A 141- $\mu\text{W}$  high-voltage MEMS gyroscope drive interface circuit based on flying capacitors," *IEEE J. Solid-State Circuits*, vol. 54, no. 2, pp. 511–523, Feb. 2019.
- [33] Y. Zhao et al., "A sub- $0.1^\circ/\text{h}$  bias-instability split-mode MEMS gyroscope with CMOS readout circuit," *IEEE J. Solid-State Circuits*, vol. 53, no. 9, pp. 2636–2650, Sep. 2018.
- [34] B. Eminoglu and B. E. Boser, "Chopped rate-to-digital FM gyroscope with 40 ppm scale factor accuracy and 1.2 dph bias," in *IEEE Int. Solid-State Circuits Conf. (ISSCC) Dig. Tech. Papers*, Feb. 2018, pp. 178–180.
- [35] H. Lee, A. Partridge, and F. Assaderaghi, "Low jitter and temperature stable MEMS oscillators," in *Proc. IEEE Int. Freq. Control Symp.*, May 2012, pp. 1–5.
- [36] Y. Zhao et al., "A sub- $\mu\text{g}$  bias-instability MEMS oscillating accelerometer with an ultra-low-noise read-out circuit in CMOS," *IEEE J. Solid-State Circuits*, vol. 50, no. 9, pp. 2113–2126, Sep. 2015.

- [37] D. Djekic *et al.*, "A 0.1% THD, 1-M $\Omega$  to 1-G $\Omega$  tunable, temperature-compensated transimpedance amplifier using a multi-element pseudo-resistor," *IEEE J. Solid-State Circuits*, vol. 53, no. 7, pp. 1913–1923, Jul. 2018.
- [38] M. H. Perrott *et al.*, "A low area, switched-resistor based fractional-N synthesizer applied to a MEMS-based programmable oscillator," *IEEE J. Solid-State Circuits*, vol. 45, no. 12, pp. 2566–2581, Dec. 2010.
- [39] H. Chandrakumar and D. Marković, "A high dynamic-range neural recording chopper amplifier for simultaneous neural recording and stimulation," *IEEE J. Solid-State Circuits*, vol. 52, no. 3, pp. 645–656, Mar. 2017.
- [40] X. Wang *et al.*, "A 0.4  $\mu\text{g}$  bias instability and 1.2  $\mu\text{g}/\sqrt{\text{Hz}}$  noise floor MEMS silicon oscillating accelerometer with CMOS readout circuit," *IEEE J. Solid-State Circuits*, vol. 52, no. 2, pp. 472–482, Feb. 2017.
- [41] P. G. R. Silva *et al.*, "An IF-to-baseband  $\Sigma\Delta$  modulator for AM/FM/IBOC radio receivers with a 118 dB dynamic range," *IEEE J. Solid-State Circuits*, vol. 42, no. 5, pp. 1076–1089, May 2007.
- [42] L. Breems, E. van der Zwan, and J. Huijsing, "A 1.8-mW CMOS  $\Sigma\Delta$  modulator with integrated mixer for A/D conversion of IF signals," *IEEE J. Solid-State Circuits*, vol. 35, no. 4, pp. 468–475, Apr. 2000.
- [43] S. Pan and K. A. A. Makinwa, "A wheatstone bridge temperature sensor with a resolution FoM of 20 fJ.K<sup>2</sup>," in *IEEE Int. Solid-State Circuits Conf. (ISSCC) Dig. Tech. Papers*, Feb. 2019, pp. 186–188.
- [44] S. Billa, A. Sukumaran, and S. Pavan, "Analysis and design of continuous-time delta-sigma converters incorporating chopping," *IEEE J. Solid-State Circuits*, vol. 52, no. 9, pp. 2350–2361, Sep. 2017.



**Arthur Campos de Oliveira** (Graduate Student Member, IEEE) received the B.Sc. degree in electrical engineering from the Federal University of Pampa, Alegrete, Brazil, in 2015, and the M.Sc. degree in microelectronics from the Federal University of Rio Grande do Sul, Porto Alegre, Brazil, in 2017. He is currently pursuing the Ph.D. degree with the Delft University of Technology, Delft, The Netherlands.

His current research interests include the design analog and mixed-signal circuits, power management, and sensor interfaces.



**Singing Pan** (Member, IEEE) received the B.Sc. degree in electronic engineering from Tsinghua University, Beijing, China, in 2013, and the M.Sc. and Ph.D. degrees (*cum laude*) in electrical engineering from the Delft University of Technology, Delft, The Netherlands, in 2016 and 2021, respectively.

He was a Post-Doctoral Researcher with the Electronic Instrumentation Laboratory, Delft University of Technology. In 2022, he joined Tsinghua University as an Assistant Professor. His research interests include smart sensors, CMOS frequency references,

and delta-sigma ( $\Delta\Sigma$ ) modulators.

Dr. Pan was a recipient of the ADI Outstanding Student Designer Award in 2019 and the IEEE SSCS Predoctoral Achievement Award in 2020. He serves as a Reviewer for IEEE JOURNAL OF SOLID-STATE CIRCUITS (JSSC), IEEE TRANSACTIONS ON CIRCUITS AND SYSTEMS—I: REGULAR PAPERS (TCAS-I), IEEE TRANSACTIONS ON CIRCUITS AND SYSTEMS—II: EXPRESS BRIEFS (TCAS-II), IEEE TRANSACTIONS ON INSTRUMENTATION AND MEASUREMENT (TIM), *Sensors* Journal, and IEEE TRANSACTIONS ON VERY LARGE SCALE INTEGRATION (VLSI) SYSTEMS (T-VLSI).



**Remco J. Wiegerink** received the M.Sc. degree in electrical engineering from the University of Twente, Enschede, The Netherlands, in 1988, on the subject of a fully integrated ultralow frequency low-pass filter for offset cancelling in integrated audio amplifiers, and the Ph.D. degree in electrical engineering from the University of Twente in 1992, on the subject of MOS translinear circuits.

From 1992 to 1995, he was with the Applied Physics Department, University of Twente, where he was engaged in the design of a superconducting flash analog-to-digital converter with GHz sampling frequency, where he joined the Transducer Science and Technology Group in 1995. Since 1995, his research has focused on mechanical microsensors, electronic interfacing of sensors, and packaging. Highlights include a silicon load cell with distributed capacitive readout, distributed thermal flow sensors using resistor arrays, an RF power sensor based on sensing the electrical force between the signal line and a suspended electrode, flow sensors based on the flow sensing hairs of crickets, and micro-Coriolis flow sensors. He is currently an Associate Professor with the Integrated Devices and Systems Group, MESA + Institute for Nanotechnology, University of Twente. He is the (co)author of two books, several book chapters, and more than 250 journal and conference papers.



**Kofi A. A. Makinwa** (Fellow, IEEE) received the B.Sc. and M.Sc. degrees from Obafemi Awolowo University, Ife, Nigeria, in 1985 and 1988, respectively, the M.E.E. degree from the Philips International Institute, Eindhoven, The Netherlands, in 1989, and the Ph.D. degree from the Delft University of Technology, Delft, The Netherlands, in 2004.

From 1989 to 1999, he was a Research Scientist with Philips Research Laboratories, Eindhoven, where he worked on interactive displays and digital recording systems. In 1999, he joined the Delft

University of Technology, where he is currently an Antoni van Leeuwenhoek Professor and the Head of the Microelectronics Department. His research interests include design of mixed-signal circuits, sensor interfaces, and smart sensors. This has led to 17 books, more than 300 technical articles, and more than 30 patents.

Dr. Makinwa is a member of the Royal Netherlands Academy of Arts and Sciences. He was the Analog Subcom Chair of ISSCC and has served on the program committees of several other IEEE conferences. He is currently one of the organizers of the Advances in Analog Circuit Design Workshop and the IEEE Sensor Interfaces Meeting. He is an ISSCC Top-Ten Contributor (with more than 60 articles), and was a co-recipient of 17 best paper awards, from the IEEE JOURNAL OF SOLID-STATE CIRCUITS (JSSC) (2), ISSCC (5), and the VLSI Circuits Symposium (2), among others. He has also served the Solid-State Circuits Society as a distinguished lecturer and as an elected member of its Adcom.